
This is an electronic reprint of the original article.
This reprint may differ from the original in pagination and typographic detail.

Mitin, Dmitry M.; Bolshakov, Alexey D.; Neplokh, Vladimir; Mozharov, Alexey M.; Raudik, Sergei A.; Fedorov, Vladimir V.; Shugurov, Konstantin Yu; Mikhailovskii, Vladimir Yu; Rajanna, Pramod M.; Fedorov, Fedor S.; Nasibulin, Albert G.; Mukhin, Ivan S.

Novel design strategy for GaAs-based solar cell by application of single-walled carbon nanotubes topmost layer

Published in:
Energy Science and Engineering

DOI:
[10.1002/ese3.713](https://doi.org/10.1002/ese3.713)

Published: 01/08/2020

Document Version
Publisher's PDF, also known as Version of record

Published under the following license:
CC BY

Please cite the original version:
Mitin, D. M., Bolshakov, A. D., Neplokh, V., Mozharov, A. M., Raudik, S. A., Fedorov, V. V., Shugurov, K. Y., Mikhailovskii, V. Y., Rajanna, P. M., Fedorov, F. S., Nasibulin, A. G., & Mukhin, I. S. (2020). Novel design strategy for GaAs-based solar cell by application of single-walled carbon nanotubes topmost layer. *Energy Science and Engineering*, 8(8), 2938-2945. <https://doi.org/10.1002/ese3.713>

This material is protected by copyright and other intellectual property rights, and duplication or sale of all or part of any of the repository collections is not permitted, except that material may be duplicated by you for your research use or educational purposes in electronic or print form. You must obtain permission for any other use. Electronic or print copies may not be offered, whether for sale or otherwise to anyone who is not an authorised user.



RESEARCH ARTICLE

Novel design strategy for GaAs-based solar cell by application of single-walled carbon nanotubes topmost layer

Dmitry M. Mitin^{1,2} | Alexey D. Bolshakov¹ | Vladimir Neplokh^{1,2} |
Alexey M. Mozharov¹ | Sergei A. Raudik¹ | Vladimir V. Fedorov^{1,2} |
Konstantin Yu. Shugurov¹ | Vladimir Yu. Mikhailovskii³ | Pramod M. Rajanna^{4,5} |
Fedor S. Fedorov⁴ | Albert G. Nasibulin^{4,5} | Ivan S. Mukhin^{1,6}

¹Saint Petersburg Academic University, St. Petersburg, Russia

²Peter the Great St. Petersburg Polytechnic University, St. Petersburg, Russia

³Saint Petersburg State University, St. Petersburg, Russia

⁴Skolkovo Institute of Science and Technology, Moscow, Russia

⁵Aalto University, Espoo, Finland

⁶ITMO University, St. Petersburg, Russia

Correspondence

Dmitry M. Mitin, Saint Petersburg Academic University, 8 Khlopina, Bld. 3A, St. Petersburg 194021, Russia.
Email: mitindm@mail.ru

Funding information

Russian Science Foundation, Grant/Award Number: 17-19-01787 and 19-79-00074

Abstract

Attempts to improve solar cells efficiency touch all its constituents and are directly related to their fabrication protocols. While the most promising material platform for high efficiency photovoltaic devices is still III-V semiconductors, introduction of novel materials like single-walled carbon nanotubes (SWCNTs), which are characterized by unique combination of conductivity and transparency, might greatly yield the device performance. Here, for the first time, we present the results of the fabrication and characterization of a thin-film GaAs solar cell with a SWCNT top contact. We examine the contact between the SWCNT film and the semiconductor structure by means of the optical and electron beam-induced current techniques. The fabricated device demonstrates better performance, that is, increased power conversion efficiency from 10.6% to 11.5% when compared to the cell with the traditional metal contact grid, stemming from the enhanced photocurrent collection efficiency and low parasitic light absorption in the emitter layer. We envision future prospects to exploit the multifunctionality of the SWCNTs in fabrication of highly efficient photovoltaic devices including flexible solar cells.

KEY WORDS

EBIC, EQE, GaAs, OBIC, solar cell, SWCNT

A continuous increase in world energy consumption forces further developments to be made in the field of primary power sources with the aim to improve their efficiency. However, the final cost of the produced power should generally be a result of (a) complexity of the device manufacturing protocols including cost of materials, (b) its long-term operation, and (c) its performance.

Nowadays, great power generation capabilities are attributed to photovoltaic (PV) devices and solar cells (SC) primarily represented by the poly- and monocrystalline silicon (Si)-based solar modules.¹ Despite the indubitable dominance of Si-based PV devices, other semiconductor materials such as gallium arsenide (GaAs) allow achieving higher conversion efficiency and enable fabrication of lightweight,

This is an open access article under the terms of the Creative Commons Attribution License, which permits use, distribution and reproduction in any medium, provided the original work is properly cited.

© 2020 St. Petersburg Academic University. *Energy Science & Engineering* published by the Society of Chemical Industry and John Wiley & Sons Ltd.

flexible, highly efficient, radiation resistant, environmental, and temperature stable thin-film solar cells. These benefits make them a better option to fulfill the demand of a high-power supply in specific applications, such as satellites, solar vehicles,² and bioimplants.³⁻⁵ While the epitaxial growth techniques of GaAs are generally established and thin-film device structures are optimized to gain the best solar cell performance,⁶⁻⁸ the topmost contact impedes the most efficient overall power conversion as optical and electrical losses in the topmost layers make sufficient impact on the efficiency of the modern PV devices.

Conventionally, a semiconductor SC top contact is a metal grid⁹ providing reasonable transparency, but requiring a high doping of the SC surface layer to provide efficient photocurrent collection. Such an architecture facilitates high rates of carrier recombination thereby effectively decreasing the device performance. Moreover, heavy doping of the semiconductor layer and the deposition of metal grid demand technologically energy-consuming process, thus significantly affecting the final device cost.

In order to address these problems, many promising materials have been tested so far, for example, semitransparent metals,¹⁰ poly(3,4-ethylenedioxythiophene) polystyrene sulfonate (PEDOT:PSS),¹¹ graphene,¹² silver nanowires,¹³ conductive oxides,¹⁴ and carbon nanotubes.¹⁵ PEDOT:PSS has been widely used as a hole transport layer in organic, Si hybrid, and perovskite SCs.¹⁶⁻¹⁸ However, to overcome low lateral conductivity and mobility of such conductive polymers, an alternative material like SWCNTs has been found to be beneficial either in its original form or as composite with various conductive polymers like PEDOT:PSS, P3HT, and P3OT.¹⁹⁻²²

In this case, aerosol synthesized SWCNTs might be preferred option, as they are characterized by the unique combination of optoelectronic properties, flexibility, chemical stability, and simple transfer protocols which allows to cover large surface area (up to sq. meters).²³⁻²⁵ A thin SWCNT film can be used as a transparent conductive electrode for the hole collection in SCs.^{22,26} Moreover, modern technologies are capable of fabrication of both metallic and semiconducting SWCNT layers that can be potentially implemented not only as a passive element (as an effective transparent electrode on the front surface of the SC), but also as a part of active region, for example, the emitter layer, which produces the built-in electrical field for photogenerated carriers separation, and wide bandgap optical window. Recently, SWCNT layer was used as an p-type layer of a Schottky barrier-based SC.^{27,28} The reported SWCNT/Si SC demonstrates low open-circuit voltage and rather low energy conversion efficiency. The discrepancy of work function between SWCNTs and Si or GaAs limits the use of SWCNTs as an emitter layer of the SC. Still, SWCNTs are characterized with relatively low bandgap, which significantly restricts their application as a wide bandgap window

material. However, due to their optoelectrical properties, the SWCNTs could help greatly improve the performance of SC when applied as a transparent contact layer material.

In this work, we fabricate and thoroughly characterize GaAs-based SC with the top contact SWCNT layer and compare its performance with conventional SC with the metal grid contact to demonstrate potential of the SWCNTs use to enhance the PV efficiency via optimization of the electronic transport and control of the optical properties.

In order to demonstrate the advantages of the SWCNT-based top contact approach, we compare the cell performance of the conventional cell with a traditional metal contact grid. We have fabricated two GaAs-based SCs: (a) simple GaAs SC, which we further denote as “basic” (see Figure 1A), and (b) the one with the SWCNTs (see Figure 1B). The design of the cells has been chosen similar to the one described in the literature.^{29,30} The fabricated SCs do not feature back surface field (BSF) layer or antireflection coating (ARC) to make the structure rather simple, required to carry out interpretation of unambiguous characterization results for precise SWCNT performance evaluation.

We employ the simplest model to evaluate the effect of SWCNTs. According to the basic SC structure numerical calculation results (see Figure 1C), a thick 400 nm emitter layer provides efficient current collection by the metal grid. Smaller emitter thickness results in the higher current density in the emitter layer (see Figure 1D), which leads to photocurrent losses facilitated by large distance between the grid fingers (which will be discussed further). In the case of the SWCNTs use, the top contact provides good carrier collection along the whole SC surface and high lateral conductivity (see Figure 1E), so the emitter layer thickness can be sufficiently decreased. We have chosen a 30 nm thick emitter for the SWCNT SC, considering that further thinning leads to propagation of the build-in electric field into the AlGaAs window layer, leading to generation of undesired electron-hole pairs in AlGaAs.³¹ The rest of the SC structure in terms of the layers sequence, thickness, composition, and doping is similar to the basic SC design (see Figure 1A,B). The details of calculation and the simplified energy band diagram of SC modified with CNT layer are given in Supporting information.

The basic SC has highly doped GaAs contact layer which was selectively etched after the metal grid fabrication (see Figure 1A) to suppress the parasitic light absorption in the layer.³² Due to the absence of the essential potential barrier between the SWCNTs and the window layer (which is confirmed with the results of contact resistance test,³³ presented in Supporting information) and since the SWCNTs cover the entire SC surface, the contact layer is absent in the SWCNT SC (see Figure 1B). For this cell, GaAs capping layer was synthesized to protect the AlGaAs window from oxidation during the fabrication and was completely etched prior to

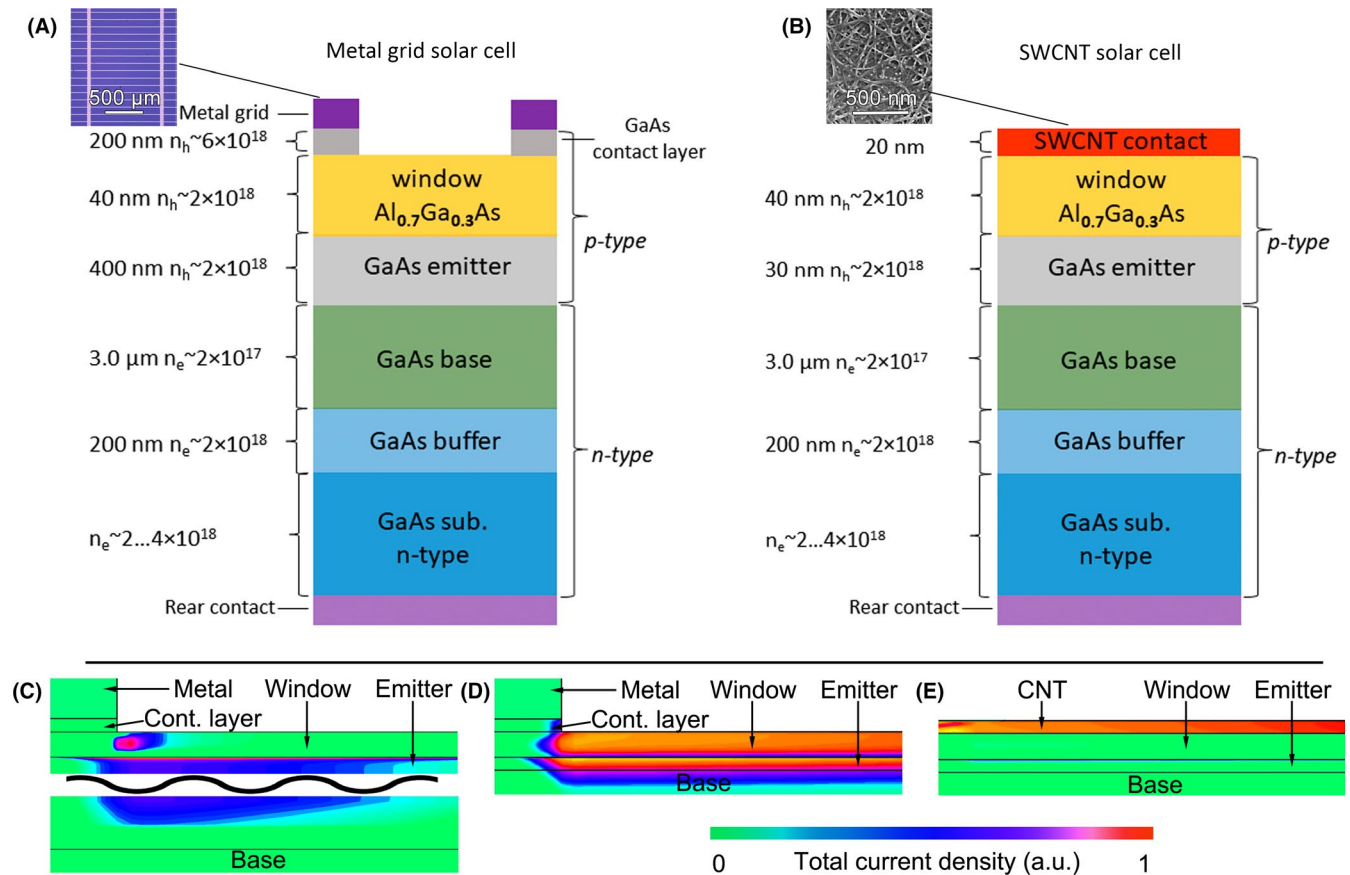


FIGURE 1 Schematic representation of the fabricated SCs with (A) metal grid (and its top-view optical image on the inset) and (B) SWCNT top contact (and its top-view SEM image in the inset). Results of the numerical calculation of the photogenerated current distribution within (C) basic SC with 400 nm emitter—the lateral current flows mainly through the emitter, (D) basic SC with 30 nm emitter—the lateral current of higher density flows mainly through the emitter and the wide bandgap window, and (E) SWCNT SC with 30 nm emitter—the current flows predominantly in the SWCNT layer providing an effective lateral carrier transport

the SWCNTs transfer. Before applying the contact grid and SWCNT, the surface of both type SCs was passivated with wet chemical treatments in hydrazine-sulfide solution to decrease the surface state density in accordance with the procedure described in.^{34,35}

Ni/AuGe (3/300 nm) rear contact was deposited onto the backside of the GaAs wafer. Pattern of the Cr/Au 40/200 nm top metal grid of the basic SC with conventional design³⁶ was defined using optical lithography technique. The metallic contacts were treated with rapid thermal annealing in nitrogen atmosphere in order to achieve linear volt-ampere characteristic between the semiconductor transport layer and metal. In accordance with measurements (not presented here), the contact resistance between p-GaAs and Cr/Au metal bars was 10^{-5} Ohm cm^2 . Details of heterostructure fabrication are presented in Supplementary section.

The SWCNT SC was thermally annealed after the rear contact deposition by the same procedure as the basic sample. Prior to the SWCNT transfer, the protective thin GaAs capping layer was etched with citric acid solution just as described earlier.³² The SWCNT thin films were dry transferred

from the nitrocellulose filter to the SC front surface.^{22,37} Note that, used transfer method allows to cover large area samples.²³ In accordance with our previous studies,³⁸ it is required to use SWCNT with a sheet resistance in the range of (10-100) Ω/sq to achieve maximum SC efficiency. We chose SWCNTs layer of ~ 20 nm thickness with integral 90% transparency in the visible range and 300 Ω/sq ²² initial sheet resistance, providing good trade-off between the conductivity and optical transmittance of the SWCNT film. After the dry-transfer of SWCNTs on the SC front surface, the gold chloride (AuCl_3) dissolved in ethanol solution was drop-casted on the SWCNTs film reducing the sheet resistance drastically to ~ 40 Ω/sq .^{37,39-41} SWCNT film transparency corresponded to the metal grid coverage.

PV characteristics of the fabricated SCs were evaluated via measurement of the current-voltage characteristic (I-V) by the four probe method with a use of AM1.5G⁴² solar simulator. To provide electrical contact, silver paste droplets were put directly on the metal grid and SWCNTs. External quantum efficiency (EQE) was measured with a spectrometer consisted of monochromator and photodetector.⁴³ The measured

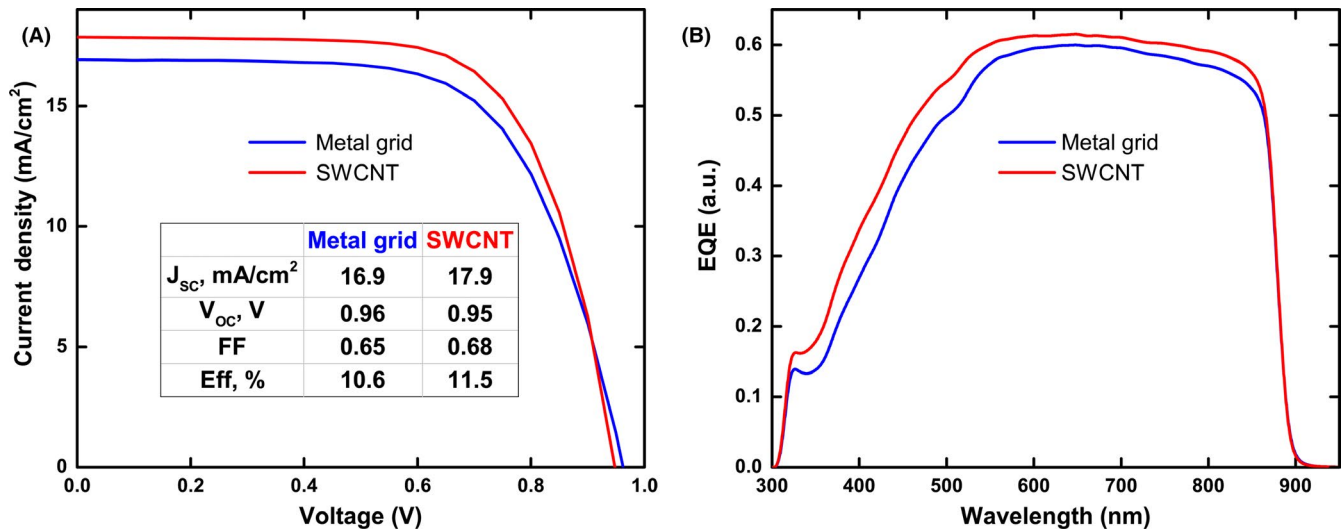


FIGURE 2 (A) I-V curves of the fabricated SCs under illumination and their summarized PV parameters (on the inset), where J_{sc} —short circuit current density, V_{oc} —open-circuit voltage, FF —fill factor, and Eff —power conversion efficiency, (B) EQE characteristics of the SCs

I-V and EQE characteristics are presented in Figure 2A,B, respectively. Figure 2A inset summarizes the main PV output characteristics of the SCs.

The measured EQE spectra (Figure 2B) demonstrate effective light absorption in 350-900 nm range typical for single-junction GaAs-based SCs.⁴⁴ The measured EQE is saturated at 60% for both types of the SCs. The low EQE is possibly due to the unoptimized design of the SCs, including the absence of the BSF and heterostructure poor crystallinity caused by the epitaxial growth flaws resulted in formation of carrier recombination centers both on the surface and point defects in bulk. Also, efficient reflection from GaAs/AlGaAs surface,⁴⁵ the absence of proper anti-reflection coating, and light-trapping optimization processing justify such low EQE.

We have observed increased EQE for the SWCNT SC when compared to the metal grid SC in the whole spectrum, especially in 350-550 nm wavelength range that leads to increase of the short circuit current density from 16.9 to 17.9 mA/cm² (see Figure 2A). The EQE rise can be associated with the thinner emitter layer: The thicker heavily doped emitter of the basic SC can affect the EQE because of the parasitic light absorption and carrier recombination. Also, enhancement of the EQE in the case of SWCNT SC can be associated with the improved carrier collection demonstrated by numerical modeling (see Figure 1C,E) and confirmed by the experimental results discussed further. On the other hand, the antireflection provided by the ~20 nm thick SWCNT layer is not significant in the visible range⁴⁶ and should not affect the EQE sufficiently. Thus, we observe increased power conversion efficiency from 10.6% to 11.5% by application of the SWCNTs, while the FF remains the same, and both SCs demonstrate typical for GaAs SCs open-circuit voltage (V_{oc}) of 0.95 and 0.96 V (Figure 2A).

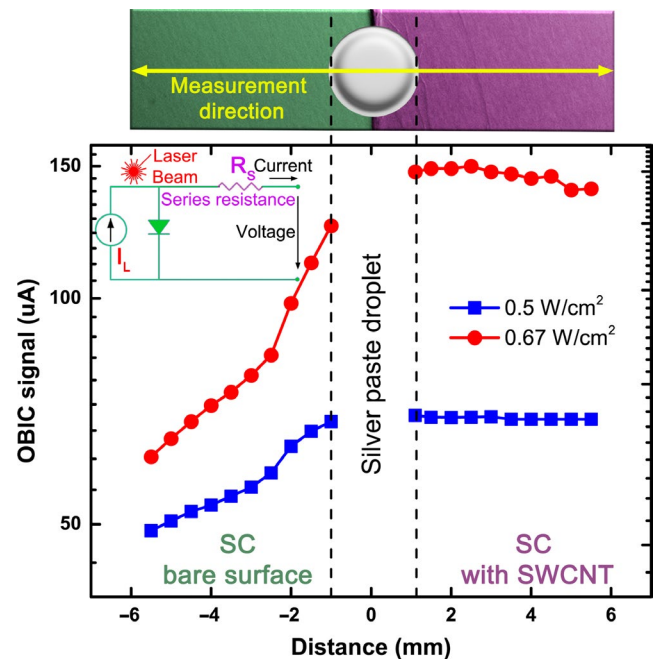


FIGURE 3 OBIC signal (presented in log scale) vs distance from the silver paste droplet at different optical beam power densities measured along the SC bare surface (left) and SC with the SWCNTs (right). SEM image of the prepared sample (presented in color for clarity) with a schematic presentation of a silver droplet and OBIC scan line. Equivalent electrical circuit representing the current flow at arbitrary illuminated point of the SC (in the inset)

To check whether the SWCNTs provide advantage of the current collection efficiency over the basic SC due to lower carriers pathway in the emitter layer, optical beam-induced current (OBIC)^{47,48} measurements have been performed in the setup equipped with automated XY-stage. We have assessed carriers' collection on the sample with the thin emitter

partially covered with the SWCNTs layer (Figure 1B). During the OBIC measurements, the laser beam has been moved along the sample surface with and without the SWCNTs with a step of 0.5 mm. The signal was collected from the bottom contact and a silver paste droplet applied to the edge of the SWCNT layer (see SEM image on the inset in Figure 3) providing measurement of the photocurrent generated at the SC surface with the SWCNT film and at the bare SC surface. The sample has been illuminated with a semiconductor laser with a wavelength of 650 nm which corresponds to the median AM 1.5G spectrum wavelength. The laser spot area was $\sim 3 \times 10^{-4} \text{ cm}^2$. The typical light intensities range of the GaAs SC operation is from 1 to 500 suns, which corresponds to power density of 0.1 to 50 W/cm^2 integrated over the spectrum. For the OBIC measurements, we took the following power densities: 0.5 W/cm^2 and 0.67 W/cm^2 . The measurements were performed at zero offset bias applied to the SC, and the results are presented in Figure 3.

The photogenerated current (OBIC signal) is maximum near the silver paste droplet, which acts as a current-collecting electrode (Figure 3). It is clearly seen that at long distance from the laser-irradiated area to the droplet, a slight current decrease (less than 10%) is observed for the SC covered with the SWCNTs and a significant current drop (up to 3 times) in the area without SWCNTs for all the illumination intensities. Moreover, in both areas, the magnitude of the relative current drop depends on the power of the incident laser beam.

To explain the origin of such OBIC signal behavior, we consider the operation of a SC in the area of laser beam illumination and outside it. At each point of the SC, an approximate equation can be considered that describes the flow of current through the SC⁴⁹:

$$I = I_0 \cdot (\exp(eV/kT) - 1) - I_L, \quad (1)$$

where I_0 is the reverse saturation current of the diode, V is a local electric potential, e and k are the electron charge and Boltzmann constant, respectively, T is local temperature, and I_L is a photogenerated current.

The first term of the right part of the Equation (1) corresponds to the injection current flowing through the diode, and the second term is attributed to the photocurrent generated in the illuminated area. Thus, the current flowing through each point of the SC can be interpreted in the terms of an equivalent electrical circuit consisting of a photocurrent source (at the illuminated point) and a diode shunting it, and the current depends on the voltage at each point (inset in Figure 3). During the OBIC measurements, the current generated at the illuminated point flows to the collection point along the upper layers of the SC (emitter, window, and SWCNT) having resistance, R_s (inset in Figure 3). The more distant the collection point from the illuminated point—the higher the resistance and, according to Ohm's law, the higher should be the voltage

at the illuminated point to provide the same photogenerated current flow. The latter leads to the local voltage increase at the illuminated point. As it can be seen from the equation, the increase in voltage leads to a nonlinear increase in the injection part of the current and reduction of the total current through the SC, which is significantly manifested when the local voltage exceeds 0.6 V (see I-V plot in Figure 2A). For a more conductive surface layer (eg, with SWCNT), the local voltage rise should be less expressed and the current should be higher. Notably, the voltage gain is directly related to the photocurrent, but not to its density, which should be reflected in the dependence of OBIC measurements on the illumination power.

The significant photocurrent decay is observed with increasing distance for the SC without the SWCNTs (see Figure 3), which, according to the proposed model, corresponds to a significant excess of the local voltage above 0.6 V. The relative decay in the photocurrent increases with the illumination power density (from 28% at 0.5 W/cm^2 to 51% at 0.67 W/cm^2).

Analysis of the OBIC current behavior along the surface covered with SWCNTs shows that at low illumination power densities, the OBIC signal does not change sufficiently with distance, and when the laser beam power density is 0.67 W/cm^2 , there is a slight photocurrent drop (5%), corresponding to insufficient local excess voltage not exceeding 0.6 V.

Thus, SC covered with the SWCNTs should be characterized by a lower surface resistance, which leads to the enhanced operation efficiency. However, this conclusion implies that SWCNT contact has a minor influence on the band structure of the SC active region, that is, heterostructures covered and uncovered with the SWCNTs differ only in terms of the surface conductivity. To remind, within the reported approach we intended to use SWCNTs contact exclusively for the current collection, and not as a part of the active region of the SC, as was previously reported in.^{27,50,51}

Deposition of the doped SWCNTs layer can potentially stimulate free carriers injection in the window and emitter layers and, consequently, affect the Fermi level at the SC surface leading to the change of the electric field distribution near the p-n junction and to the change of the photogenerated carriers collection efficiency. The latter effect can be visualized via monitoring of the change in the spatial distribution of the electron beam-induced current (EBIC) signal across the junction⁵² due to the change in the carriers separation with built-in electrical field after deposition of the SWCNTs. Note that EBIC technique provides visualization of built-in field profile with sub-100 nm resolution. Therefore, we have performed cross-sectional EBIC mapping of the sample areas covered and uncovered with the SWCNTs.

The SWCNT SC has been cleaved to obtain a flat and vertical cut edges. The absence of electrical shunts produced by the cleavage procedure has been controlled by

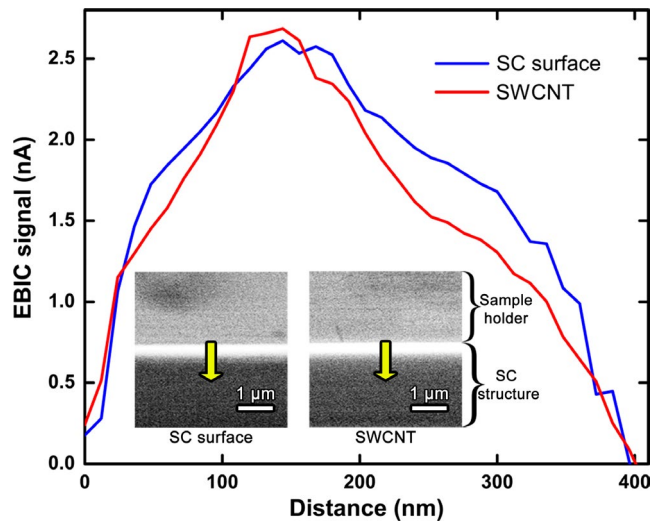


FIGURE 4 Cross-sectional EBIC profiles of the uncontacted surface area (blue curve) and the SWCNT-contacted area (red curve) of the SC; insets show EBIC bright contrast maps of the uncontacted surface area (left) and SWCNT-contacted area (right), respectively; yellow arrows indicate the EBIC signal profiling line, and their tails correspond to the SC top surface (0-coordinate of the plot)

EBIC mapping, as well as by in situ I-V measurements during the EBIC mapping. The sample has been fixed on the insulated holder, and two probes were connected to the device contacts. The measurements were carried out at 5 kV e-beam acceleration voltage with the same contacts as for I-V characterization.

We present the measured EBIC profiles corresponding to the line scans designated on the cross-sectional EBIC maps of the SC with and without the SWCNTs obtained at the same conditions in Figure 4. Zero coordinate of the EBIC profile should be related to the sample's top surface. Gray scale contrast in EBIC maps corroborates with the e-beam generated current. Profiles of the SWCNT-covered areas (red curve) typically have sharper peak compared to the uncovered areas (blue curve). However, apart from the peak sharpness, profiles of the EBIC signal from SWCNT-covered and bare SC surface areas are similar in terms of size (about 400 nm) and current value (2.5 nA) proving that SWCNTs do not sufficiently affect the band structure of the studied SC and does not form a potential barrier at the interface.

To summarize the results of OBIC and EBIC characterization, we conclude that SWCNT contact allows effective collection of the photogenerated current and has a minor impact on the properties of the SC active region. The current collection properties of SWCNTs appeared to be excessive, so even higher energy conversion efficiency rise can be achieved by decreasing of SWCNT contact area coverage, for example, by the layer patterning providing open windows in the SWCNTs layer. The proposed strategy could be applied to highly efficient flexible SCs.⁵³

To conclude, we have demonstrated fabrication of high-quality SWCNTs contact transparent electrodes suitable for III-V semiconductor PV devices. SC with SWCNT contact has shown slight increase in the short circuit current density from 16.9 to 17.9 mA/cm² and the EQE leading to 0.9% efficiency rise compared to SC with the conventional metal grid contact. The carried out OBIC and EBIC study of the SWCNT SC demonstrates good electrical contact between the SC surface and the SWCNTs as well as perfect transport properties of the latter leading to good charge carriers collection. These properties together with a very technologically simple deposition method of the SWCNT contact layer makes this material a promising alternative to the SC contacts based on metallic grid, which can be applied to a wide range of semiconductor large area PV devices including flexible thin film and structures with developed surface morphology including nanowire-based SCs.

ACKNOWLEDGMENTS

D. M. M. acknowledge the Russian Science Foundation for support of the metal contacts fabrication and OBIC investigations (project # 19-79-00074). P. M. R., F. S. F., and A. G. N. acknowledge the Russian Science Foundation for the support (synthesis and doping of SWCNTs) by project # 17-19-01787.

CONFLICT OF INTEREST

The authors declare no competing financial interest.

ORCID

Dmitry M. Mitin  <https://orcid.org/0000-0003-4517-0807>

Alexey D. Bolshakov  <https://orcid.org/0000-0001-7223-7232>

Vladimir Neplokh  <https://orcid.org/0000-0001-8158-0681>

Alexey M. Mozharov  <https://orcid.org/0000-0002-8661-4083>

Vladimir V. Fedorov  <https://orcid.org/0000-0001-5547-9387>

Vladimir Yu. Mikhailovskii  <https://orcid.org/0000-0003-1168-771X>

Pramod M. Rajanna  <https://orcid.org/0000-0002-6175-4442>

Fedor S. Fedorov  <https://orcid.org/0000-0002-2283-0086>

Albert G. Nasibulin  <https://orcid.org/0000-0002-1684-3948>

Ivan S. Mukhin  <https://orcid.org/0000-0001-9792-045X>

REFERENCES

- Green MA. Commercial progress and challenges for photovoltaics. *Nat Energy*. 2016;1(1):15015.

2. Zhao J, Wang A, Yun F, et al 20 000 PERL silicon cells for the '1996 World Solar Challenge' solar car race. *Prog Photovolt Res Appl*. 1997;5(4):269-276.
3. Song K, Han JH, Yang HC, Nam K II, Lee J. Generation of electrical power under human skin by subdermal solar cell arrays for implantable bioelectronic devices. *Biosens Bioelectron*. 2017;92:364-371.
4. Liscouet-Hanke S, Shafiei A, Lopes L, Williamson S. Proof-of-concept analysis of a supplemental solar power system for aircraft. *Aircr Eng Aerosp Technol*. 2018;90(8):1295-1304. <https://doi.org/10.1108/AEAT-08-2017-0189>
5. Vu NH, Pham T-T, Shin S. Flat concentrator photovoltaic system for automotive applications. *Sol Energy*. 2019;190:246-254.
6. Green MA, Hishikawa Y, Dunlop ED, Levi DH, Hohl-Ebinger J, Ho-Baillie AWY. Solar cell efficiency tables (version 52). *Prog Photovolt Res Appl*. 2018;26(7):427-436.
7. Kayes BM, Zhang L, Twist R, Ding I-K, Higashi GS. Flexible thin-film tandem solar cells with >30% efficiency. *IEEE J Photovolt*. 2014;4(2):729-733.
8. Khan AD, Khan AD. Optimization of highly efficient GaAs-silicon hybrid solar cell. *Appl Phys A*. 2018;124(12):851.
9. Sofia SE, Sahraei N, Mailoa JP, Buonassisi T, Peters IM. Metal grid contact design for four-terminal tandem solar cells. *IEEE J Photovolt*. 2017;7(3):934-940.
10. Chen Q, Switzer JA. Photoelectrochemistry of ultrathin, semi-transparent, and catalytic gold films electrodeposited epitaxially onto n-silicon (111). *ACS Appl Mater Interfaces*. 2018;10(25):21365-21371.
11. Bergqvist J, Österberg T, Melianas A, et al Asymmetric photocurrent extraction in semitransparent laminated flexible organic solar cells. *npj Flex Electron*. 2018;2(1):4.
12. Yoon J, Sung H, Lee G, et al Superflexible, high-efficiency perovskite solar cells utilizing graphene electrodes: towards future foldable power sources. *Energy Environ Sci*. 2017;10(1):337-345.
13. Ricciardulli AG, Yang S, Wetzelaer G-JAH, Feng X, Blom PWM. Hybrid silver nanowire and graphene-based solution-processed transparent electrode for organic optoelectronics. *Adv Funct Mater*. 2018;28(14):1706010.
14. Dai P, Lu J, Tan M, et al Transparent conducting indium-tin-oxide (ITO) film as full front electrode in III-V compound solar cell. *Chin Phys B*. 2017;26(3):037305.
15. Shastry TA, Hersam MC. Carbon nanotubes in thin-film solar cells. *Adv Energy Mater*. 2017;7(10):1601205.
16. Kim YH, Sachse C, Machala ML, May C, Müller-Meskamp L, Leo K. Highly conductive PEDOT:PSS electrode with optimized solvent and thermal post-treatment for ITO-free organic solar cells. *Adv Funct Mater*. 2011;21(6):1076-1081.
17. Zhang Y, Cui W, Zhu Y, et al High efficiency hybrid PEDOT:PSS/nanostructured silicon Schottky junction solar cells by doping-free rear contact. *Energy Environ Sci*. 2015;8(1):297-302.
18. Hou F, Su Z, Jin F, et al Efficient and stable planar heterojunction perovskite solar cells with an MoO₃/PEDOT:PSS hole transporting layer. *Nanoscale*. 2015;7(21):9427-9432.
19. Lee D-Y, Na S-I, Kim S-S. Graphene oxide/PEDOT:PSS composite hole transport layer for efficient and stable planar heterojunction perovskite solar cells. *Nanoscale*. 2016;8(3):1513-1522.
20. Jeon I, Matsuo Y, Maruyama S. Single-walled carbon nanotubes in solar cells. *Top Curr Chem*. 2018;376(1):4.
21. Fan Q, Zhang Q, Zhou W, et al Novel approach to enhance efficiency of hybrid silicon-based solar cells via synergistic effects of polymer and carbon nanotube composite film. *Nano Energy*. 2017;33:436-444.
22. Rajanna PM, Gilshteyn EP, Yagafarov T, et al Enhanced efficiency of hybrid amorphous silicon solar cells based on single-walled carbon nanotubes and polymer composite thin film. *Nanotechnology*. 2018;29(10):105404.
23. Gilshteyn EP, Lin S, Kondrashov VA, et al A one-step method of hydrogel modification by single-walled carbon nanotubes for highly stretchable and transparent electronics. *ACS Appl Mater Interfaces*. 2018;10(33):28069-28075.
24. Jariwala D, Sangwan VK, Lauhon LJ, Marks TJ, Hersam MC. Carbon nanomaterials for electronics, optoelectronics, photovoltaics, and sensing. *Chem Soc Rev*. 2013;42(7):2824-2860.
25. Li X, Guard LM, Jiang J, et al Controlled doping of carbon nanotubes with metallocenes for application in hybrid carbon nanotube/Si solar cells. *Nano Lett*. 2014;14(6):3388-3394.
26. De Nicola F, Salvato M, Cirillo C, et al 100% Internal quantum efficiency in polychiral single-walled carbon nanotube bulk heterojunction/silicon solar cells. *Carbon NY*. 2017;114:402-410.
27. Tune DD, Flavel BS, Krupke R, Shapter JG. Carbon nanotube-silicon solar cells. *Adv Energy Mater*. 2012;2(9):1043-1055.
28. Li X, Lv Z, Zhu H. Carbon/silicon heterojunction solar cells: state of the art and prospects. *Adv Mater*. 2015;27(42):6549-6574.
29. Melloch MR. High-efficiency GaAs solar cells grown by molecular-beam epitaxy. *J Vac Sci Technol B Microelectron Nanom Struct*. 1990;8(2):379.
30. Ragay FW, Leys MR, Nouwens PAM, van der Vleuten WC, Wolter JH. A MBE-grown high-efficiency GaAs solar cell with a directly deposited aluminum front contact. *IEEE Electron Device Lett*. 1992;13(12):618-620.
31. Ragay FW, Ruigrok EWM, Wolter JH. GaAs-AlGaAs heterojunction solar cells with increased open-circuit voltage. In: *Proceedings of 1994 IEEE 1st World Conference on Photovoltaic Energy Conversion - WCPEC (A Joint Conference of PVSC, PVSEC and PSEC)*, Vol. 2. IEEE; 1994:1934-1937.
32. DeSalvo GC. Etch rates and selectivities of citric acid/hydrogen peroxide on GaAs, Al_{0.3}Ga_{0.7}As, In_{0.2}Ga_{0.8}As, In_{0.53}Ga_{0.47}As, In_{0.52}Al_{0.48}As, and InP. *J Electrochem Soc*. 1992;139(3):831.
33. Reeves GK, Harrison HB. Obtaining the specific contact resistance from transmission line model measurements. *IEEE Electron Device Lett*. 1982;3(5):111-113.
34. Berkovits VL, Ulin VP, Losurdo M, Capezzuto P, Bruno G. Wet chemical treatment in hydrazine-sulfide solutions for sulfide and nitride monomolecular surface films on GaAs(100). *J Electrochem Soc*. 2005;152(5):G349.
35. Berkovits VL, Ulin VP, Tereshchenko OE, et al Chemistry of wet treatment of GaAs(111)B and GaAs(111)A in hydrazine-sulfide solutions. *J Electrochem Soc*. 2011;158(3):D127.
36. Schroder DK, Meier DL. Solar cell contact resistance—a review. *IEEE Trans Electron Devices*. 1984;31(5):637-647.
37. Tsapenko AP, Goldt AE, Shulga E, et al Highly conductive and transparent films of HAuCl₄-doped single-walled carbon nanotubes for flexible applications. *Carbon NY*. 2018;130:448-457.
38. Raudik SA, Mozharov AM, Mitin DM, et al Numerical simulation of the carbon nanotubes transport layer influence on performance of GaAs solar cell. *J Phys Conf Ser*. 2018;1124:041040.
39. Kim KK, Bae JJ, Park HK, et al Fermi level engineering of single-walled carbon nanotubes by AuCl₃ doping. *J Am Chem Soc*. 2008;130(38):12757-12761.

40. Kim SM, Kim KK, Jo YW, et al Role of anions in the AuCl₃-doping of carbon nanotubes. *ACS Nano*. 2011;5(2):1236-1242.
41. Murat A, Rungger I, Jin C, Sanvito S, Schwingenschlögl U. Origin of the P-type character of AuCl₃ functionalized carbon nanotubes. *J Phys Chem C*. 2014;118(6):3319-3323.
42. Bazzi AM, Klein Z, Sweeney M, Kroeger KP, Shenoy PS, Krein PT. Solid-state solar simulator. *IEEE Trans Ind Appl*. 2012;48(4):1195-1202.
43. Träger F, ed. *Springer Handbook of Lasers and Optics*. New York, NY: Springer; 2007.
44. Moon S, Kim K, Kim Y, Heo J, Lee J. Highly efficient single-junction GaAs thin-film solar cell on flexible substrate. *Sci Rep*. 2016;6(1):30107.
45. Aspnes DE, Kelso SM, Logan RA, Bhat R. Optical properties of Al_xGa_{1-x}As. *J Appl Phys*. 1986;60(2):754-767.
46. Maine S, Koechlin C, Rennesson S, et al Complex optical index of single wall carbon nanotube films from the near-infrared to the terahertz spectral range. *Appl Opt*. 2012;51(15):3031.
47. Wilson T, McCabe EM. Theory of optical beam induced current images of defects in semiconductors. *J Appl Phys*. 1987;61(1):191-195.
48. Galloway SA, Brinkman AW, Durose K, Wilshaw PR, Holland AJ. A study of the effects of post-deposition treatments on CdS/CdTe thin film solar cells using high resolution optical beam induced current. *Appl Phys Lett*. 1996;68(26):3725-3727.
49. Sze SM, Ng KK. *Physics of Semiconductor Devices*. Hoboken, NJ: John Wiley & Sons Inc; 2006.
50. Tune DD, Flavel BS. Advances in carbon nanotube-silicon hetero-junction solar cells. *Adv Energy Mater*. 2018;8(15):1703241.
51. Chen W, Seol G, Rinzler AG, Guo J. Carrier dynamics and design optimization of electrolyte-induced inversion layer carbon nanotube-silicon Schottky junction solar cell. *Appl Phys Lett*. 2012;100(10):103503.
52. Luke KL, Von Roos O. An EBIC equation for solar cells. *Solid State Electron*. 1983;26(9):901-906.
53. Chen H-L, Cattoni A, De Lépinau R, et al A 19.9%-efficient ultra-thin solar cell based on a 205-nm-thick GaAs absorber and a silver nanostructured back mirror. *Nat Energy*. 2019;4(9):761-767.

SUPPORTING INFORMATION

Additional supporting information may be found online in the Supporting Information section.

How to cite this article: Mitin DM, Bolshakov AD, Neplokh V, et al. Novel design strategy for GaAs-based solar cell by application of single-walled carbon nanotubes topmost layer. *Energy Sci Eng*. 2020;8:2938–2945. <https://doi.org/10.1002/ese3.713>